Chapter 9

ULTIMATE BEARING CAPACITY OF STRIP FOOTING ON UNSATURATED SANDY SOIL DUE TO TRANSIENT FLOW

9.1 INTRODUCTION

The previous two chapters describe the bearing capacity analyses of strip foundations considering the steady-state fluid flow in the vadose zone. Nevertheless, various environmental factors, such as heavy rainfall, cause time-dependent matric suction, leading to a varying stress field within the soil medium. The time-dependent variation of suction stress adversely impacts the stability of the geotechnical structures. Hence, the steady-state assumption in the vadose zone may not be technically safe or economically justifiable. Therefore, it is necessary to consider the time-varying suction stress and the corresponding changes in the effective degree of saturation while designing shallow foundations on unsaturated soil (Blake et al., 2003; Shahrokhabadi et al., 2019; Li and Yang, 2020; Fathipour et al., 2022b, 2023). However, based on the kinematics of the problem, no rigorous studies concerning the load withstand capacity of unsaturated soils under transient fluid flow are found in the literature. Thus, the utmost need of conducting a strength analysis of unsaturated soil considering the effect of spatial as well as temporal variation of matric suction profiles and incorporating the infiltration rate is quite apparent. In this chapter, a detailed investigation is carried out to examine the ultimate bearing capacity of strip foundations on variably saturated sandy soils subjected to various transient infiltration rates. The analyses are carried out with the usage of finite element upper bound limit analysis technique in conjunction with the linear optimization method.

9.2 PROBLEM STATEMENT AND DOMAIN

This study focuses on evaluating the load withstand ability of a strip footing having width *B* and resting over homogeneous, isotropic, and unsaturated sandy soil. The strip footing is rigid and rough, as depicted in Figure 9.1a. The ground surface (GS) is flat and has

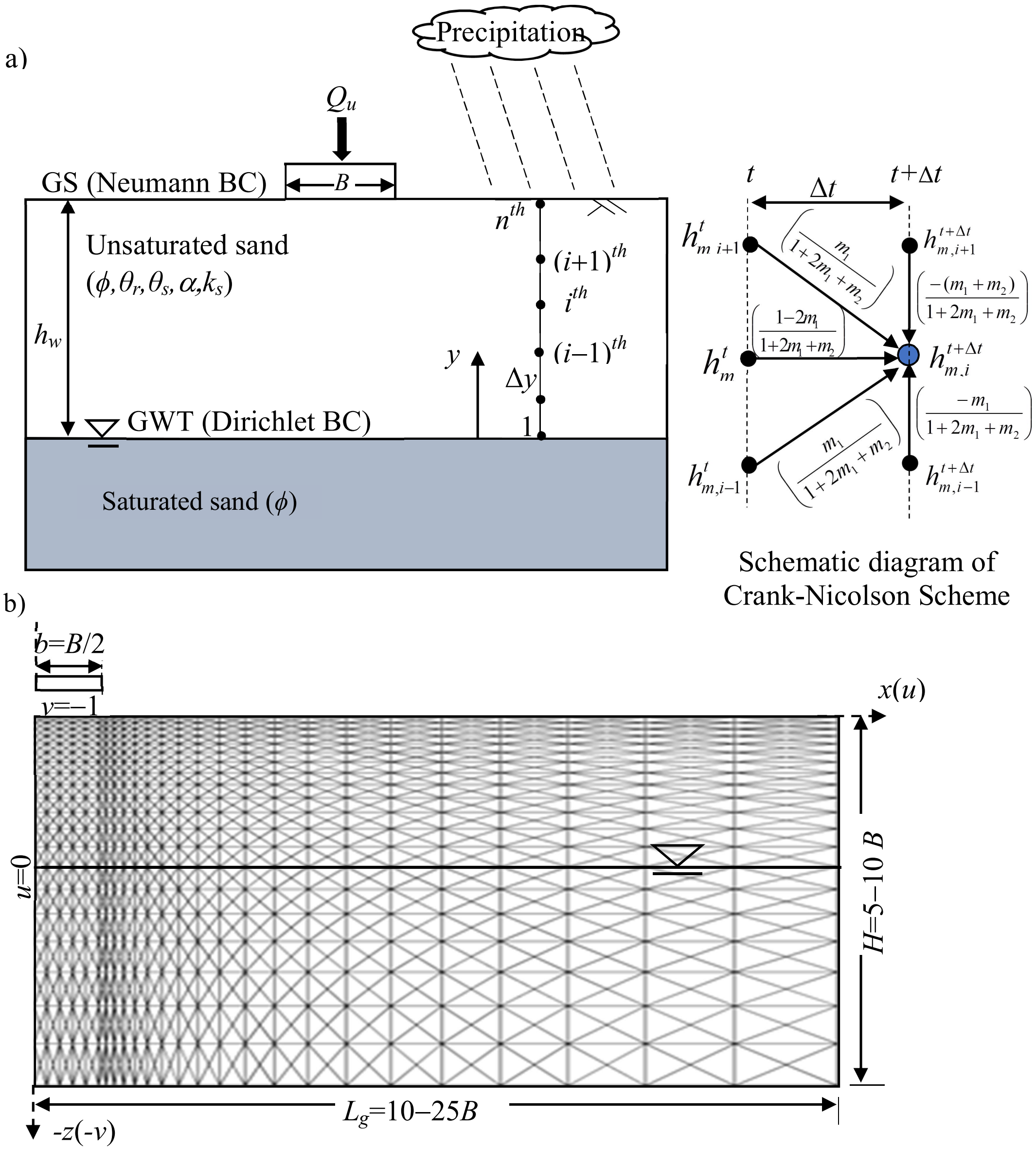

Figure 9.1 a) Domain used for strip footing resting on sandy soil; and b) mesh used for analysis.

no additional surcharge acted over it. The load acting on the strip footing is vertical and runs through the vertical axis. The groundwater table is positioned at a specific depth (h_w) beneath the ground surface. The saturated soil is described by the drained friction angle, while the vadose zone is characterized by the friction angle, unsaturated soil property functions, and permeability function. The permeability, water content, and saturation level above the GWT vary nonlinearly with the matric suction. The unsaturated soil is subjected to transient infiltration. This indicates that the matric suction above the GWT varies spatially as well as temporarily.

The domain for this analysis is shown in Figure 9.1b. The extent of the domain has been chosen to ensure that the nodal velocity patterns should remain within the domain, and any further expansion hardly alters the solutions. The horizontal extent is 5-10 times the width of the strip footing (B), while the vertical extent is 20-50 times the strip footing width. The horizontal movement is restrained along the sides AB and CD, while the bottom (BD) has zero movements in both horizontal and vertical directions. There are no constraints on the velocity along the ground surface AM and NC.

9.3 SUCTION STRESS AND ANALYSIS PROCEDURE

9.3.1 Evaluating suction stress due to transient flow

Unlike the previous chapters, where the steady-state suction stress is characterized by a closed-form equation, as mentioned in Equation (7.10), the time (t)-dependent suction stress is obtained by numerically solving the widely used partial differential equation that describes the unidirectional transient flow of pore water through homogeneous, and isotropic unsaturated soil (Richards, 1931):

$$\frac{\partial}{\partial y}\left[k(h_m)\left(\frac{\partial h_m(y,t)}{\partial y}+1\right)\right]=\frac{\partial \theta(h_m)}{\partial t};\ h_m=\text{ matric suction head}=\psi/\gamma_w \qquad (9.1)$$

Broadly, Richards equation relates the rate of change of water content to the space-gradient of soil-water potential and the hydraulic conductivity by duly considering the effects of gravity, capillarity, and diffusion process. The magnitude of permeability and volumetric water content varies with the space- and time-dependent matric suction; thus, k and θ eventually turn out to be h_m-dependent functionals. In this chapter, the functionals $k(h_m)$ and $\theta(h_m)$ are perceived to be controlled by Gardner's HCF and Gardner's SWRC models, respectively. Gardner's SWRC (Gd-SWRC) model relates θ and h_m in the following way:

$$\Theta_n = S_e = \exp\left[-\alpha\left(u_a - u_w\right)/\gamma_w\right]; \text{ where, } \Theta_n = \frac{\theta-\theta_r}{\theta_s-\theta_r} \text{ and } S_e = \frac{S-S_r}{1-S_r} \tag{9.2}$$

$$\Rightarrow \theta = \theta_r + (\theta_s - \theta_r)\exp\left[-\alpha\psi\right]; \tag{9.3}$$

Contrary to the vG-SWRC model, Gd-SWRC model depends on the volumetric water contents (θ_s, θ_r), and the α–parameter which is an inverse indicator of the air entry value. With the increase in α, the desaturation zone begins earlier, and eventually, the boundary effect zone becomes narrower. The desaturation rate gets controlled by the saturated- and residual-state volumetric water content. Due to the temporal fluctuation of water content, the vadose zone exhibits an inconsistent rate of pore water flow. Following the Gd-HCF model, the hydraulic conductivity above the groundwater table is represented as:

$$k = k_s \exp\left(-\alpha\psi\right); \; k_s = \text{saturated hydraulic conductivity}$$

Plugging Equations (9.2 and 9.3) into Equation 9.1, the following nonlinear parabolic partial governing differential equation is obtained (as shown in Appendix-E.1).

$$\left[\frac{\partial^2 h_m}{\partial y^2} + \alpha\left(\frac{\partial h_m}{\partial y}\right)^2\right] + \alpha\frac{\partial h_m}{\partial y} = \frac{\alpha(\theta_s-\theta_r)}{k_s}\frac{\partial h_m}{\partial t} \tag{9.4}$$

Equation (9.4) must be satisfied everywhere within the chosen domain ($0<y<h_m$) subjected to the following initial condition and the boundary constraints.

Initial conditions: $h_m(y,0)=y$ (9.5a)

Boundary conditions (BCs): (i) Head (Dirichlet) BC @ GWT: $h_m(0,t)=0$ (9.5b)

(ii) Flux (Neumann) BC @GS: $\left[k(h_m)\left(\frac{\partial h_m}{\partial y}+1\right)\right]_{y=h}=q$

(9.5c)

The stated initial value problem (IVP) is being solved by employing the Crank-Nicolson (1947) scheme of the finite difference method. Crank-Nicolson (1947) is a widely used semi-implicit numerical technique that provides computational flexibility and high accuracy. This scheme is unconditionally stable and guarantees 2nd order accuracy in both time and space. The domain is spatially discretized with 80 grid points as illustrated in Figure 9.1. The nonlinear differential equation is required to be satisfied at each grid point except the two extreme boundary points. The discretized form of the equation at any arbitrary i^{th} grid point is shown in Appendix E.2. To simplify the computational process, the second term in the governing differential equation (i.e., the square of the first-order derivative term) is evaluated in the known (previous) time step. Thus, the nonlinear PDE eventually gets converted into an algebraic linear form consisting of three unknown terms. The simultaneous sets of linear equations obtained from each grid point finally result in the following matrix form: $\boldsymbol{A}\boldsymbol{H}_m^{t+\Delta t}=\boldsymbol{B}^t$; here, the coefficient matrix, $\boldsymbol{A}$, is the function of Gd-SWRC model parameters (α, θ_s, and θ_r), user-defined depth-increment (Δy), and time-increment (Δt) whereas, the right-hand side vector, $\boldsymbol{B}$, depends on the matric suction values at the previous time step. Therefore, the component of the $\boldsymbol{B}$ vector keeps changing as the numerical simulations advance along the time scale; nevertheless, the $\boldsymbol{A}$ matrix remains constant. The $\boldsymbol{A}$ matrix consists of two non-dimensional terms, m_1 and m_2. In order to prevent the spurious oscillations, small increments (Δy and Δt) are chosen, so that non-dimensional terms do not become excessively high. The detailed numerical formulations are mentioned in Appendix- E. The simultaneous sets of linear equations are solved by using the Gauss elimination technique. After obtaining the matric suction head, the suction stress is obtained as follows:

$$\sigma^s = -\psi S_e = h_m(y,t)\gamma_m \exp\left[-\alpha h_m(y,t)\right] \tag{9.6}$$

Hence, unlike the preceding chapters, the suction stress profiles will be space- and time-dependent.

9.3.2 Variation of the Suction Stress Profiles

Corresponding to different types of unsaturated sands, Figure 9.2 depicts the variation of normalized matric suction (ψ_{norm}) and suction stress (σ^s_{norm}) profiles in the vadose zone; the normalization is done with respect to the overburden pressure measured at the GWT. Figures 9.2a and 9.2b correspond to α=0.7, whereas Figures 9.2c and 9.2d present the variation of ψ_{norm} and σ^s_{norm} pertain to α=0.9; the rest of the chosen Gd-SWRC parameters are: $\theta_s = 0.41$, $\theta_r = 0.05$. The water table is considered 4m below the ground surface. The figures are drawn for various (i) infiltration rates, namely, $q/k_s = 0.1$, 0.5, and 1.0, and (ii) three different infiltration durations, namely, t=0 day, 4 days, and 8 days. In the presence of q, the matric suction profile becomes curvilinear adjacent to the ground surface. With the advancement in infiltration duration, the matric suction profiles decrease continuously and move towards the no-suction state (i.e. saturation state). Notably, the approaching rate of the ψ line (towards the zero-suction line) is remarkably higher when the infiltration rate is extreme (i.e. $q/k_s = 1$). At t=0 day, the ground surface remains in the residual state and exhibits the highest matric suction and eventually the least effective saturation. As the infiltration duration increases, the saturation level near the GS also increases resulting in the suppression of the matric suction and the evolution of a pronounced peak point on the matric suction profile. The development of the peak point happens more prominently for the high infiltration rate. With the passage of infiltration time, this peak point moves away from the GS. Comparing Figure 9.2b and 9.2d, it can be inferred that the curvature of the σ^s profiles beyond the peak point becomes higher for high α value. Figure 9.2b presents the normalized suction stress profiles. One can observe that interpreting the matric suction profiles is more straightforward than its suction stress counterpart. The matric suction is a function of space and time, whereas the suction stress is functional of ψ and S_e. The nonlinearity of ψ and S_e curves further complicates the σ^s profiles over time. The infiltration rate hardly influences the σ^s profiles near the GWT at the initial days of infiltration. However, if the infiltration continues for a prolonged time, the σ^s curves evolved from the various infiltration rates are visibly different even near the GWT. The spread of the σ^s -profiles appear to be quite random and no conclusive argument can be drawn with respect to the infiltration duration and rate. In the ascending order of the spread of the σ^s profiles at the GS:

(i) $\sigma^s\big|_{@q/k_s=1} > \sigma^s\big|_{@q/k_s=0.5} > \sigma^s\big|_{@q/k_s=0.1}$ (@ t= 4 days)

(ii) $\sigma^s\big|_{@q/k_s=0.5} > \sigma^s\big|_{@q/k_s=0.1} > \sigma^s\big|_{@q/k_s=1}$ (@ t= 8 days)

This is observed irrespective of the α parameter. Nevertheless, the curvilinearity of the suction stress profiles near the ground surface becomes quite higher for higher α. This can be explained by the fact that both the matric suction and suction stress are influenced by the infiltration rate and duration, but their responses are opposite, and the degree of influence differs substantially.

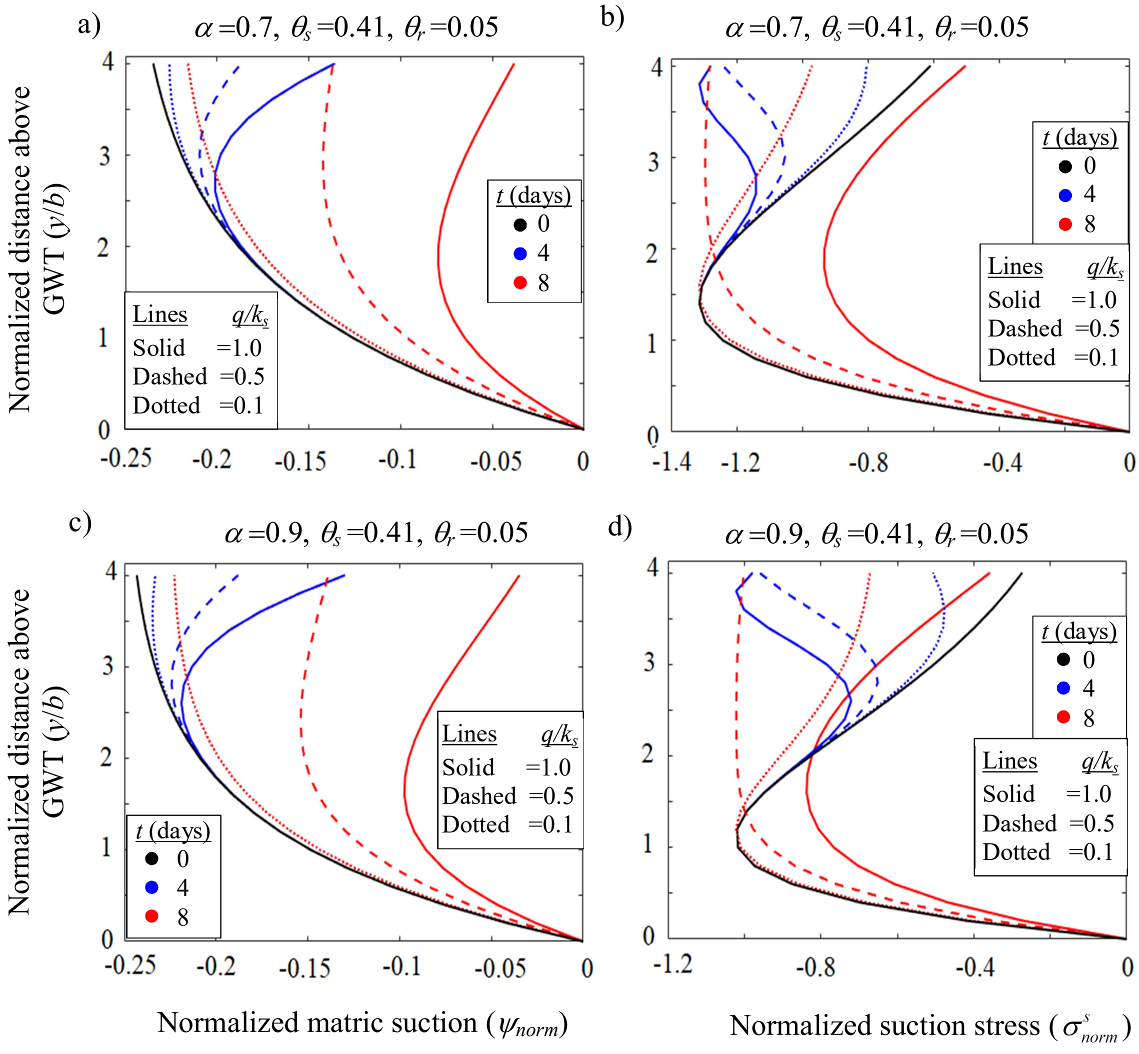

Figure 9.2 The profiles of the normalized (a,c) matric suction and (b,d) suction stress for an unsaturated sand layer under transient infiltration with α equals (a-b) 0.7; and (c-d) 0.9.

Figure 9.3 illustrates a comparison between the analytical solutions provided by Shahrokhabadi et al. (2019) based on the Laplace transformation and the approximate solutions obtained from the finite difference scheme. The curves are compared at different time, namely, t = 1, 2, 4, 6, and 8 days. There is a reasonable agreement of the and σ^{s}_{norm} curves with that of the reported one. The region between the GS and the peak point exhibits a slight difference in the analytical and numerical σ^{s} values; nonetheless, the discrepancies are insignificant in the vicinity of the GWT. Moreover, these deviations decrease over time.

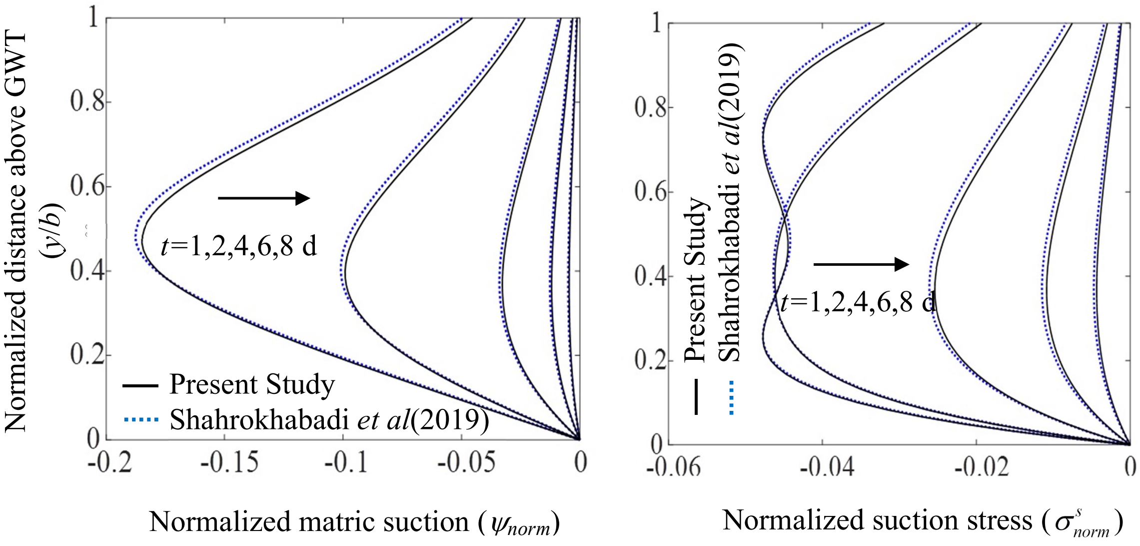

Figure 9.3 A comparative study of the present numerical solutions with the analytical solutions of Shahrokhabadi *et al.* (2019) in terms of: (a) ψ_{norm} ; and (b) σ^s_{norm} curves.

9.3.3 Analysis

Two numerical analyses are carried out in tandem for computing the transient UBC: firstly, the semi-implicit finite difference technique is implemented for achieving the suction stress vectors at different time, and then the UB-FELA is adopted to compute the ultimate bearing capacity (p_u). The procedure of obtaining p_u, based on the transient water flow, remains the same as provided in Section 7.3. The only difference is to consider the temporal suction stress profiles. It requires mentioning that the intercept of the MC failure envelope on the shear stress axis and the size of the MC failure circles also varies with the change in spatial position and infiltration duration. The soil below and above the water table are analyzed by considering different effective stress formulations:

Saturated State Effective Stress: $\sigma'_{ij} = \sigma_{ij} - u_w \delta_{ij}$

Unsaturated State Effective Stress: $\sigma'_{ij} = \sigma_{ij} - u_a \delta_{ij} - \sigma^s \delta_{ij}$

For the sake of brevity, the detailed explanation is not being mentioned here. The obtained results are mentioned in the next section.

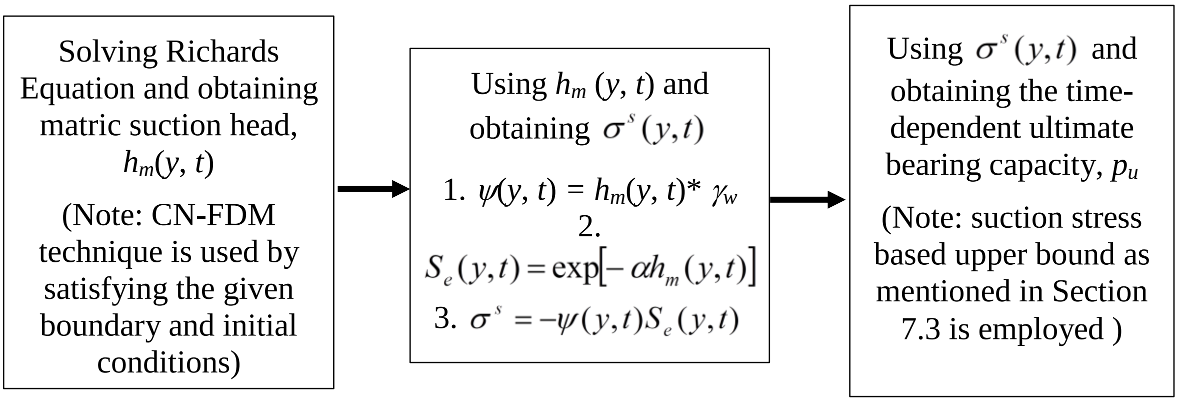

Solving Richards Equation and obtaining matric suction head, $h_m(y, t)$

(Note: CN-FDM technique is used by satisfying the given boundary and initial conditions)

Using h_m (y, t) and obtaining $\sigma^s(y,t)$

1. $\psi(y, t) = h_m(y, t)^* \gamma_w$
2. $S_e(y,t) = \exp[-\alpha h_m(y,t)]$
3. $\sigma^s = -\psi(y,t) S_e(y,t)$

Using $\sigma^s(y,t)$ and obtaining the time-dependent ultimate bearing capacity, p_u

(Note: suction stress based upper bound as mentioned in Section 7.3 is employed)

9.4 RESULTS AND DISCUSSION

9.4.1 Transient ultimate Bearing Capacity

The chosen hydromechanical parameters are as follows:

SWRC model $\Rightarrow$ Gd-SWRC parameters: $\alpha = 0.7$, θ_s=0.41, θ_r =0.05.

HCF model $\Rightarrow$ Gd-HCF (One parameter model) parameter: $\alpha = 0.6, 0.8$.

Frictional strength: ϕ=30°, 35°,40°,45°.

Flow ratios: q/k_s = 0.10, 0.25, 0.50, 0.75, and 1.0.

Water table position: h_w/b =1, 2, 3, and 4.

The graphs are plotted in terms of normalized bearing capacity; the normalization is done with respect to γB. Figures 9.4 to 9.7 display the variation of the normalized bearing capacity ($p_u/\gamma B$) with respect to time (days) and corresponding to different GWT position; Figures 9.4, 9.5, 9.6, and 9.7 present the temporal variation of $p_u/\gamma B$ curves for four different ϕ's: ϕ=30°, ϕ=35°, ϕ=40°, and ϕ=45°. Figure 9.8 shows the increment of UBC with frictional strength for two different infiltration rate (q/k_s=

0.1, 1.0) and two different GWT positions. Figure 9.9 presents the impact of α on the UBC curves. The following observations are noted:

a) The unsaturated bearing capacity is always higher than its saturation counterpart.

b) Unlike the steady-state flow, the UBC presented over here significantly varies with respect to infiltration duration and rate. It was earlier observed in Chapters 7 and 8 that the infiltration duration and rate had no impact on the steady-state suction stress profiles of coarse-grained soils with low AEV. Nevertheless, the matric suction head obtained from Richards equation depends both on q and t, even for high values of α (α >0.1). Regardless of the frictional strength, unsaturated soil properties, and infiltration duration, the computed $p_u/(\gamma B)$ always appears to be higher for a lower percolation rate. For instance, corresponding to ϕ=35°, h_w/b =3, and t=4 days, the magnitude of $p_u/(\gamma B)$ pertains to q/k_s = 0.10, and q/k_s = 1.0 are 278 kPa and 336 kPa, respectively. The reduction of the UBC corresponding to a relatively high infiltration rate is because of the moving of the suction stress profile towards the zero-suction (vertical) line over time.

c) The computed $p_u/(\gamma B)$ further gets influenced by the fluctuations of GWT. Irrespective of the flow rate, frictional strength, unsaturated soil properties, and infiltration duration, the UBC increases remarkedly by the lowering of the GWT. For an instance, corresponding to ϕ=40°, q/k_s = 0.50, and t=2 days, lowering of GWT from h_w/b=1 to h_w/b=4 enhances the UBC from 240 kPa to 1153 kPa.

d) Not only the magnitude of $p_u/(\gamma B)$, but the trend of the time-dependent UBC curves also varies drastically by the location of the GWT. When the GWT is close to the GS (i.e. h_w approximately less than 2), the $p_u/(\gamma B)$ curves continuously reduce and approach towards a horizontal plateau. The rate of this reduction is enormously high for extreme infiltration. When the GWT is remarkably away

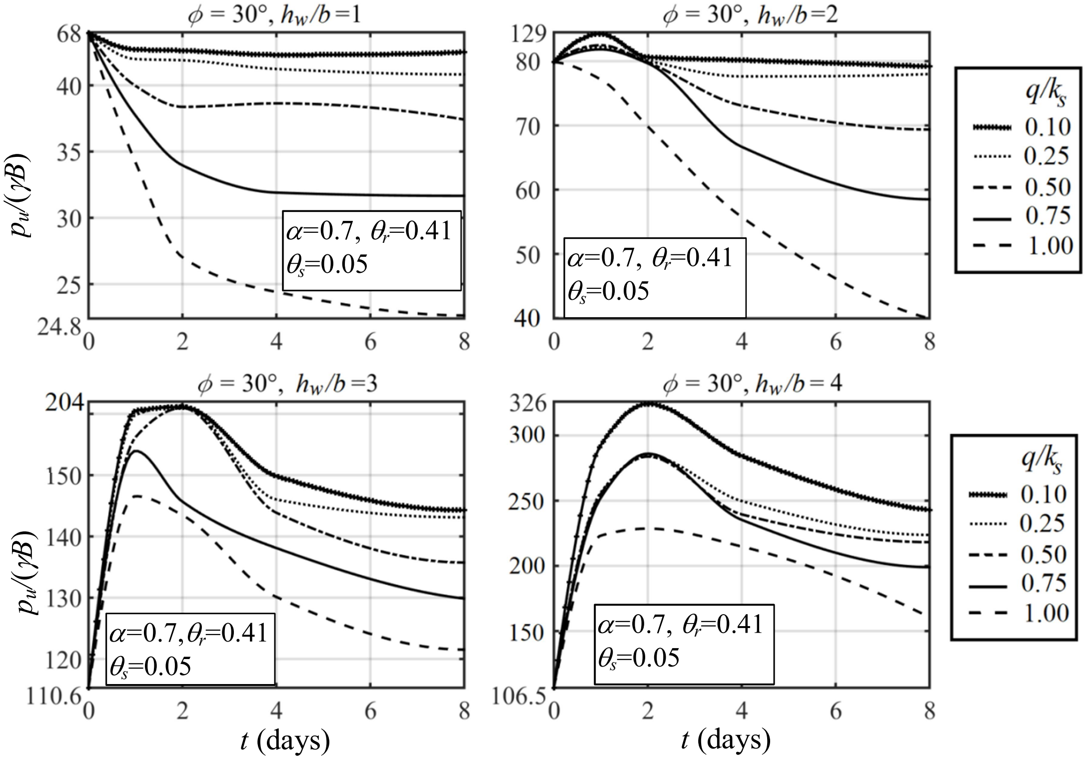

Figure 9.4 The temporal variation of $p_u/(\gamma B)$ for strip footing resting on unsaturated sand (ϕ=30°) with: a) h_w/b=1; b) h_w/b=2; c) h_w/b=3; d) h_w/b=4.

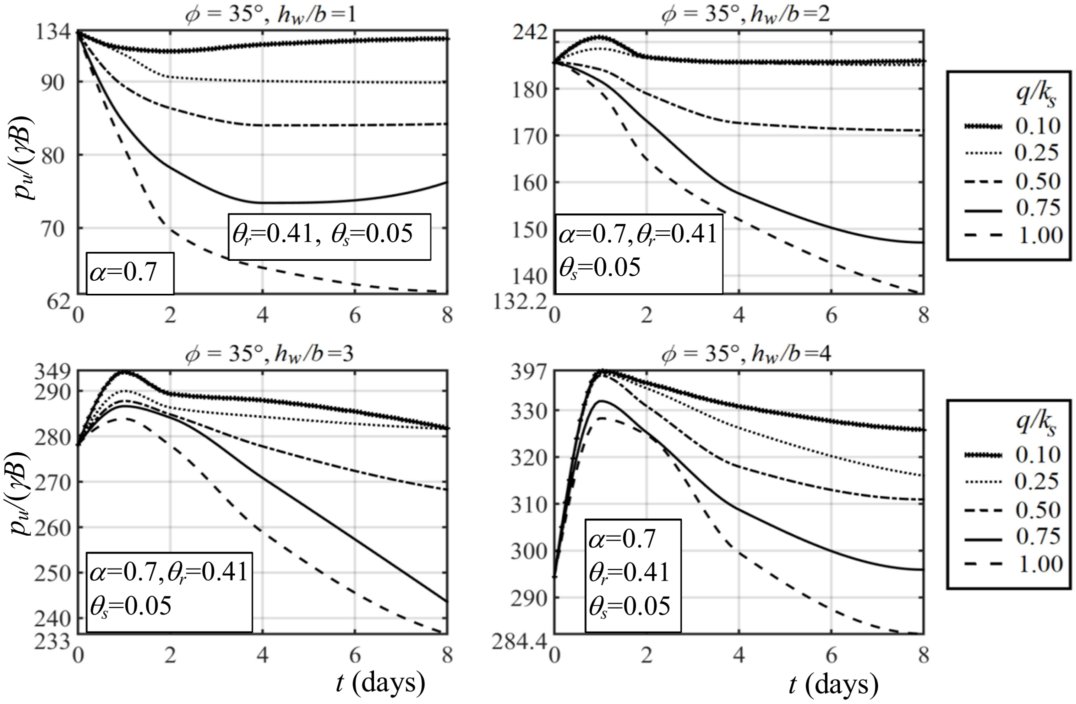

Figure 9.5 The temporal variation of $p_u/(\gamma B)$ for strip footing resting on unsaturated sand (ϕ=35°) with: a) h_w/b=1; b) h_w/b=2; c) h_w/b=3; d) h_w/b=4.

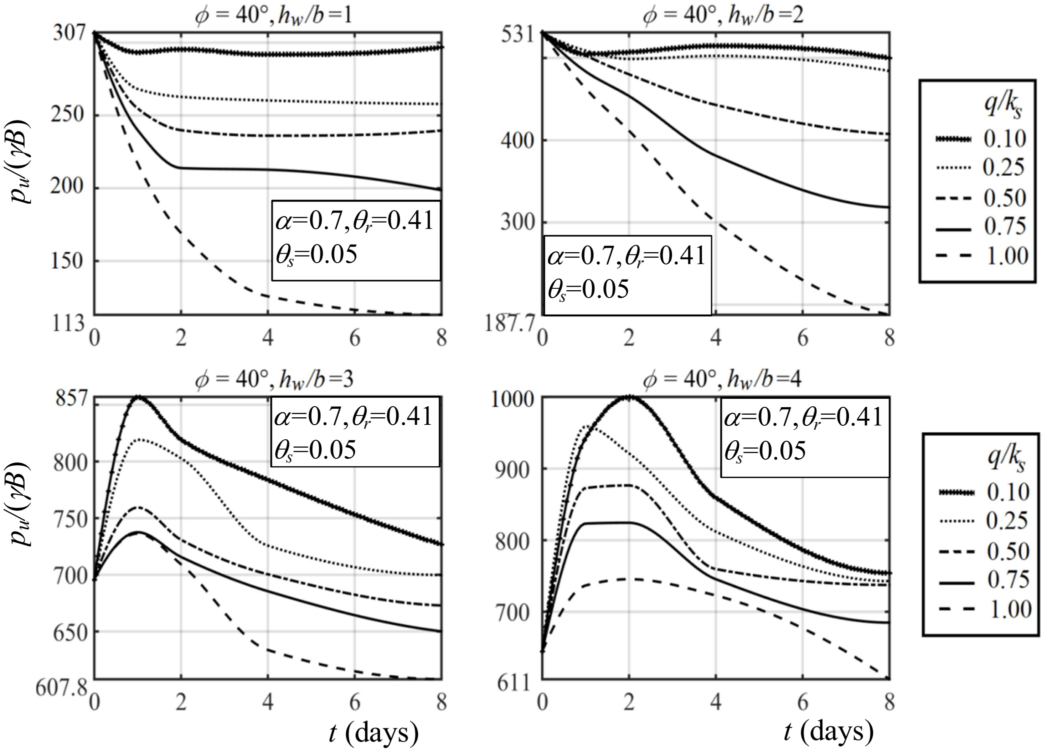

Figure 9.6 The temporal variation of $p_u/(\gamma B)$ for strip footing resting on unsaturated sand (ϕ=40°) with: a) h_w/b=1; b) h_w/b=2; c) h_w/b=3; d) h_w/b=4.

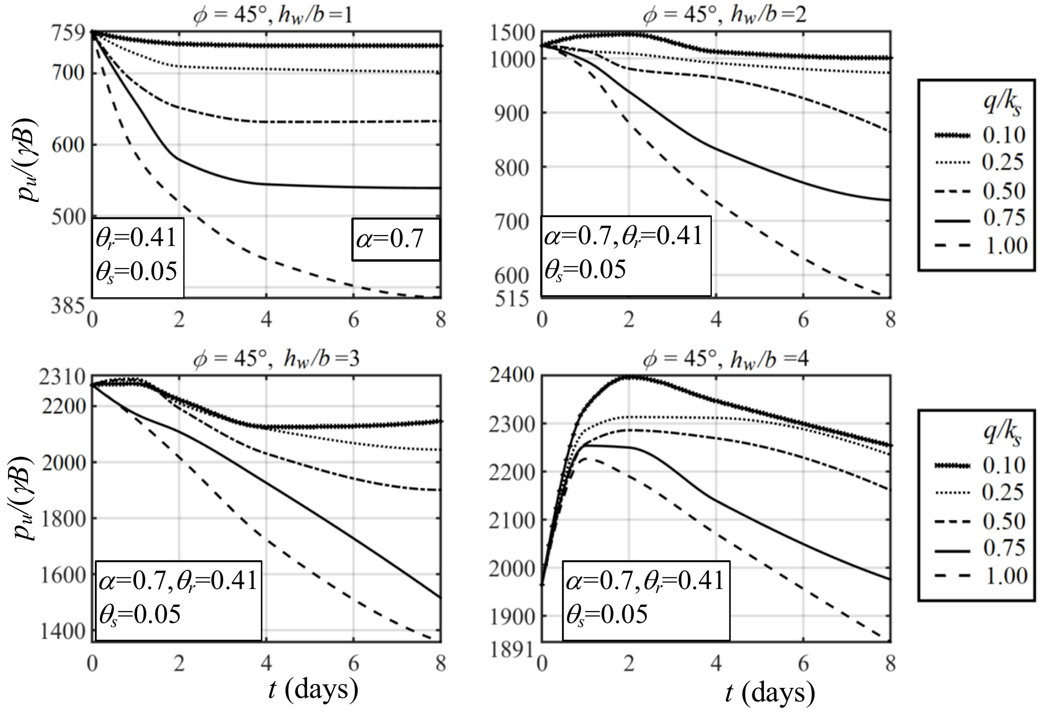

Figure 9.7 The temporal variation of $p_u/(\gamma B)$ for strip footing resting on unsaturated sand (ϕ=45°) with: a) h_w/b=1; b) h_w/b=2; c) h_w/b=3; d) h_w/b=4.

from the GS, the $p_u/(\gamma B)$ curves initially increase, attain a peak value at a certain infiltration duration, and thereafter exhibit a reverse trend. This phenomenon can be explained by the extent of the vadose zone and the change of saturation state near the ground surface due to the infiltration. The spread of the vadose zone is substantially less for h_w/b=1. The infiltration process starts saturating the soil. And, as the vadose zone is relatively shallow, the influence of the suction on the UBC does not dominate much. Nevertheless, when the GWT is located much below the GS, the domination of the suction on the UBC is quite high up to a certain time; beyond that, the saturation process adjacent to the top surface suppresses the suction-stress-induced-enhanced bearing capacity.

e) The time at which the maximum bearing capacity is achieved, is designated here as 'critical time' and symbolized as t_{cr}. The t_{cr} appears to be increasing with decreasing infiltration rate.

f) The computed $p_u/(\gamma B)$ further increases nonlinearly with the increase in frictional strength as shown in Figure 9.8. The degree of nonlinearity becomes more prominent with the lowering of the GWT. The nonlinear UBC profiles can be idealized as the bilinear profiles having two different slopes: a gentle slope (roughly between 30° and 40°) and a steep slope (beyond 40°). The steepness of the UBC profiles appears at a relatively lower friction angle when h_w/b is higher and q/k_s is lower. The fluctuation of GWT seems to be more impactful than the variation of the infiltration rate.

g) Figure 9.9 shows the normalized UBC profiles for two different α's: α =0.6, and α =0.8. The rest of the input parameters (ϕ=35°, θ_s =0.41, θ_r =0.05, and h_w/b = 4) are taken to be constant. The UBC profiles are plotted with respect to time corresponding to different flow ratios: q/k_s = 0.10, 0.50, and 1.0. The sandy soil having relatively higher AEV exhibits the fooling characteristics: (a) higher UBC, (b) pronounced peak point, (c) faster attainment of t_{cr}, (d) post-peak concavity, and (e) distinct impact of q/k_s.

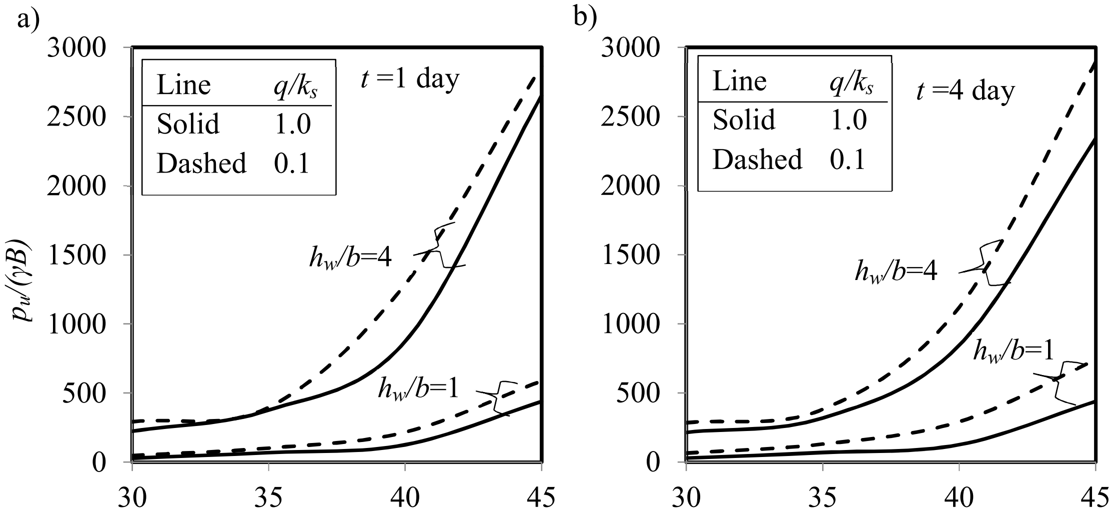

Figure 9.8 The variation of normalized bearing capacity ($p_u/\gamma B$) of strip footing with respect to the friction angle (ϕ) for: a) t =1 day; b) t = 4 days.

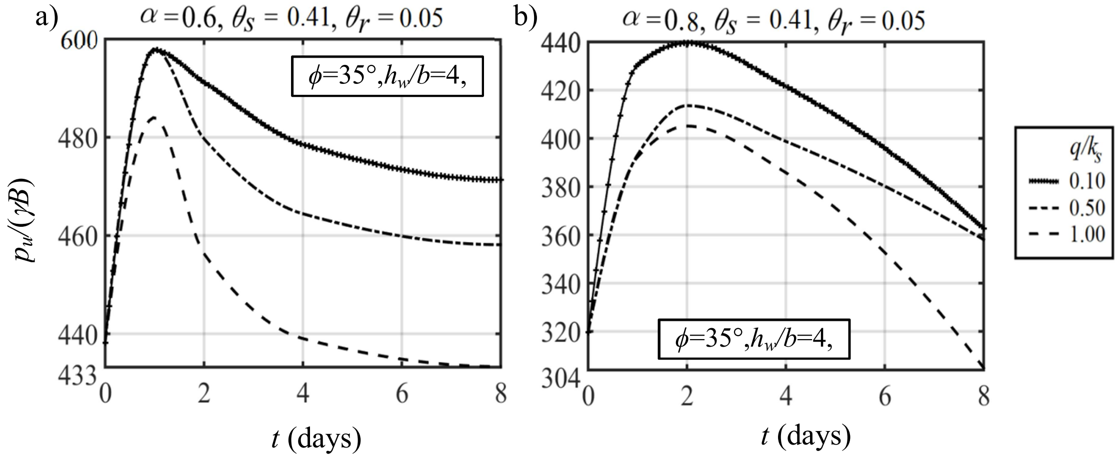

Figure 9.9 The temporal variation of normalized bearing capacity ($p_u/\gamma B$) of strip footing resting on unsaturated sand (ϕ= 35°) with: (a) α=0.6, θ_r=0.41, θ_s=0.05; (b) α=0.8, θ_r=0.41, θ_s=0.05.

9.4.2 Nodal Velocity Pattern

Figures 9.10–9.11 illustrate the nodal velocity patterns developed within the soil domain at the collapse state; Figure 9.10 shows the effect of infiltration duration and Figure 9.11 presents the influence of α parameter on the velocity contours. The velocity contour depicts the magnitude and direction of soil particle movement. These patterns are generated for different loading configurations and unsaturated soil properties. Within the soil domain, a curvilinear zone of influence is identified around the footing, where the absolute magnitudes of the nodal velocities are significantly higher compared to the rest of the soil; this indicates the extent of the failure zone. Regardless of the chosen input parameters, two observations are consistent. Firstly, the velocities along the ground surface near the footing edge are notably higher than the velocities directly below the footing base. Secondly, velocity discontinuities are primarily concentrated near the footing edge and gradually diminish at a distance away from the footing edge. Figure 9.10 represents the velocity contour at three different time: $t = 0$ day, 4 days, and 8 days; the other chosen input parameters are: $\phi=45°$, $\alpha=0.7$, $\theta_r=0.41$, $\theta_s=0.05$, $q/k_s=1$, and $h_w/b=2$. For the chosen case, the size of the failure zone reduces with increasing time. This is because of the decreasing trend of suction stress profiles with time. Nevertheless, the magnitude of the velocity vectors near the footing edge escalates with the passage of infiltration duration.

Figure 9.11 illustrates the velocity distribution of a strip footing on dense sandy soil ($\phi=40^\circ$) with varying values of α, namely, $\alpha=0.6$, $\alpha=0.7$, and $\alpha=0.8$. The contours are drawn for $\theta_r=0.41$, $\theta_s=0.05$, and $h_w/b=2$. As the α value increases, the area of influence zone decreases, and the concentration of velocity vectors near the footing edge significantly increases. This explains why the bearing capacity is higher for $\alpha=0.6$ in comparison to $\alpha=0.8$.

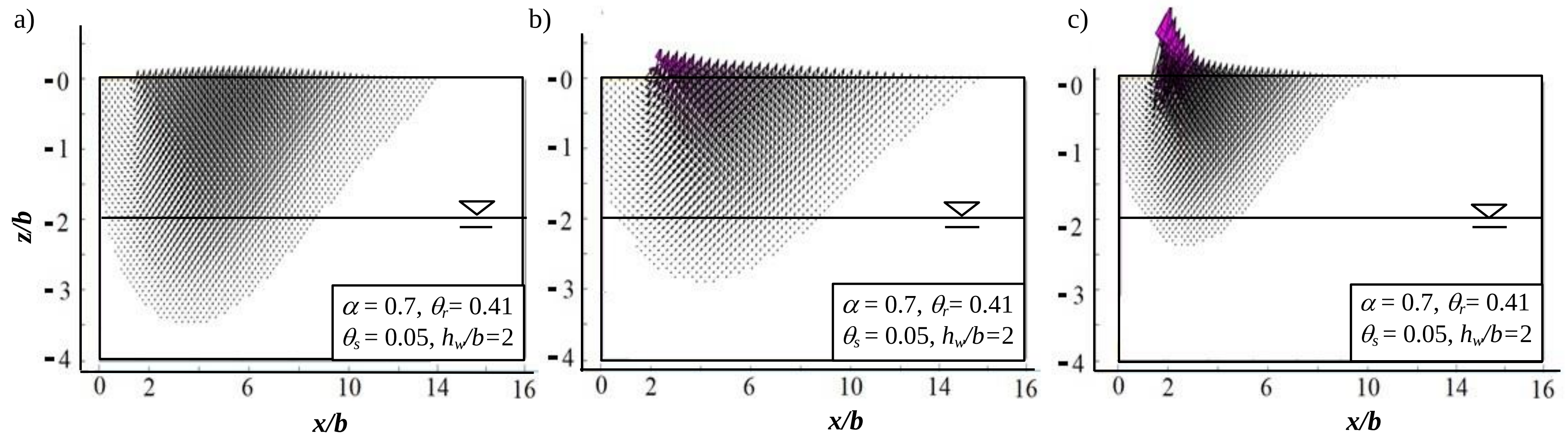

Figure 9.10 The nodal velocity pattern for strip footing on unsaturated sands with $\phi = 45^{\circ}$ corresponding to: a) $t = 1$ day; b) $t = 4$ days c) $t = 8$ days.

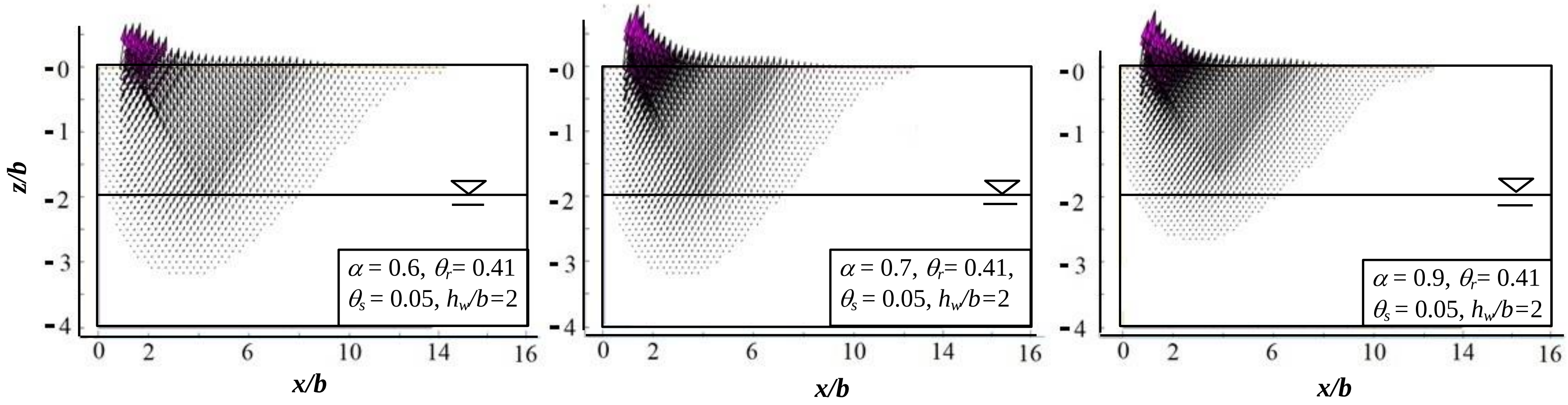

Figure 9.11 The nodal velocity pattern for strip footing on s unsaturated sands with $\phi = 40^{\circ}$ corresponding to: a) $\alpha = 0.6$; b) $\alpha = 0.7$ c) $\alpha = 0.9$.

Figure 9.12 represents the effect of infiltration rate on the extent and intensity of the nodal velocity pattern developed at the collapse state at t = 1day. Three different infiltration rates are considered for the purpose of investigations. They are: $q/k_s = 0.1$, $q/k_s = 0.5$, and $q/k_s = 1$. The GWT is positioned at $h_w/b = 1$ and the rest of the chosen hydromechanical properties are: $\phi = 35°$, $\alpha = 0.7$, $\theta_r = 0.41$, $\theta_s = 0.05$. With the increase in infiltration rate, the overall spread of the velocity contour decreases to a significant extent; this decrement appears to be more in the vertical direction than its lateral counterpart. The reduction in the velocity contour zone with the increasing in infiltration rate further supports the finding of lower UBC under extreme rainfall conditions.

Figure 9.13 illustrates the nodal velocity pattern for unsaturated sandy soil having $\phi = 35°$, $\alpha = 0.7$, $\theta_r = 0.41$, $\theta_s = 0.05$, and for $t = 1$, $q/k_s = 1$. The effects of variation of water depth on contours are presented by considering three GWT positions: h_w/b = 1, 2, and 3. The lowering of water table exhibits larger size of nodal velocity contour; this observation corroborates the attainment of higher UBC for deeper GWT. Further, the concentration of velocity discontinuities near the footing edge substantially reduces as the water table goes down. For relatively deeper water table, the velocity vectors appear to have almost uniform distribution in the influencing zone.

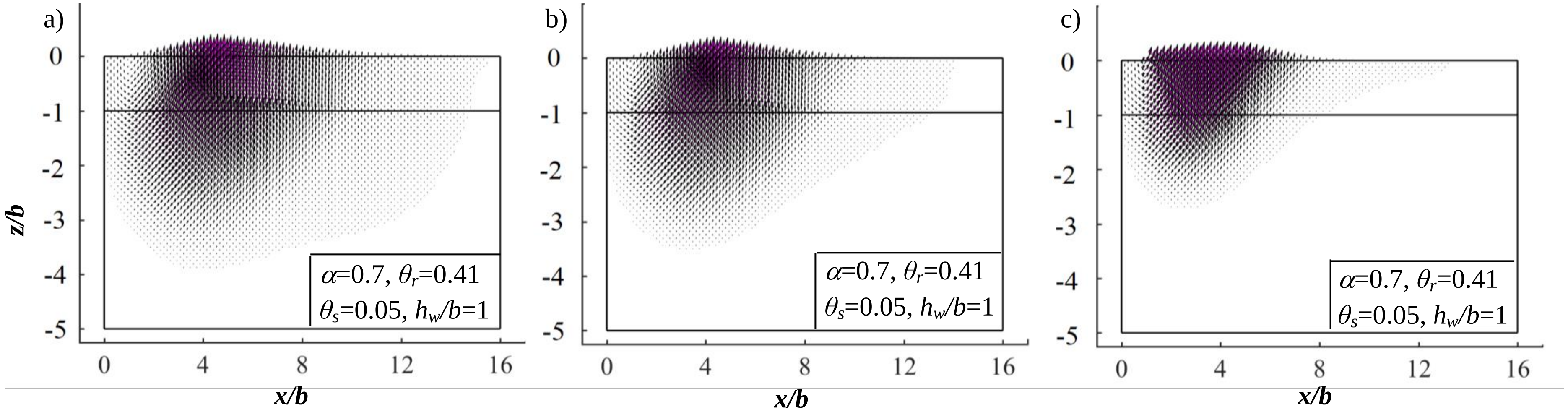

Figure 9.12 The nodal velocity pattern for strip footing on unsaturated sand with ϕ = 35° and t =1 day corresponding to: a) $q/k_s = 0.1$; b) $q/k_s = 0.5$; c) $q/k_s = 1$.

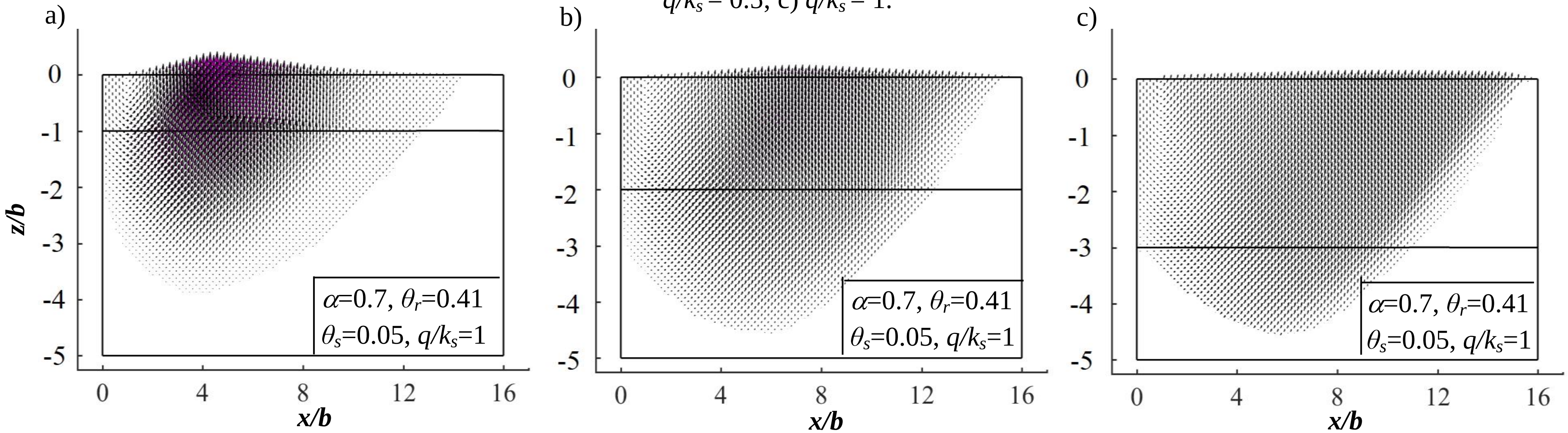

Figure 9.13 The nodal velocity pattern for strip footing on unsaturated sand with ϕ = 35° and t =1day corresponding to: a) $h_w/b = 1$; b) $h_w/b = 2$; c) $h_w/b = 3$.

9.5 SUMMARY

This study analyzed footings founded on unsaturated cohesionless soil under transient infiltration. A rigorous finite element upper bound study is conducted by employing Gardner’s SWRC model, Gardner’s HCF model, Richards transient equation, the concept of suction stress, Modified Mohr-Coulomb theory. The partially saturated soils often experience a transient flow state, which is a prevalent hydrological occurrence in the lifespan of geostructures. By factoring in the suction stress that changes over time, it becomes possible to monitor the stress field's limit state during rainfall and infiltration. The combined effect of infiltration duration and rate, unsaturated soil properties, soil’s shear strength on the transient bearing capacity are discussed elaborately. The results are presented in terms of normalized bearing capacity. The findings of this study are crucial for designing and analyzing shallow foundations, as the footing's ultimate bearing capacity changes significantly during the infiltration process.